Hydrides of Laves type Ti–Zr alloys with enhanced H storage capacity as advanced metal hydride battery anodes

Ika Dewi Wijayanti [a, b, c, **], Roman Denys [a], Suwarno [c], Alexey A. Volodin [d], M.V. Lototskyy [e], Matylda N. Guzik [f], Jean Nei [g], Kwo Young [g], Hans Jørgen Roven [b], Volodymyr Yartys [a, *]

[a] Institute for Energy Technology, Kjeller, Norway
[b] Norwegian University of Science and Technology, Trondheim, Norway
[c] Department of Mechanical Engineering, ITS, Surabaya, Indonesia
[d] Institute of Problems of Chemical Physics RAS, Chernogolovka, 142432, Russia
[e] University of the Western Cape, South Africa
[f] University of Oslo, Blindern, Oslo, Norway
[g] BASF/Battery Materials-Ovonic, Rochester Hills, USA

ARTICLE INFO

ABSTRACT

The present work was focused on the studies of the effect of variation of stoichiometric composition of Ti–Zr based $AB_{2\pm x}$ Laves phase alloys by changing the ratio between A (Ti + Zr) and B (Mn + V + Fe + Ni) components belonging to both hypo-stoichiometric ($AB_{1.90}$, $AB_{1.95}$) and over-stoichiometric ($AB_{2.08}$) alloys further to the stoichiometric $AB_{2.0}$ composition to optimize their hydrogen storage behaviours and performances as the alloy anodes of nickel metal hydride batteries.

$AB_{2-x}La_{0.03}$ Laves type alloys (A = $Ti_{0.15}Zr_{0.85}$; B = $Mn_{0.64-0.69}V_{0.11-0.119}Fe_{0.11-0.119}Ni_{1.097-1.184}$; x = 0, 0.05 and 0.1) were arc melted and then homogenized by annealing.

The studies involved probing of the phase-structural composition by X-Ray diffraction (XRD), together with studies of the microstructural state, hydrogen absorption–desorption and thermodynamic characteristics of gas–solid reactions and electrochemical charge-discharge performance, further to the impedance spectroscopy characterization. The alloys were probed using scanning electron microscopy (SEM), energy dispersive spectroscopy (EDS), and XRD.

These studies concluded that the alloys contained the main C15 FCC Laves type AB_2 intermetallic co-existing with a secondary C14 hexagonal Laves phase and a small amount of LaNi intermetallic. The gaseous H storage capacity and electrochemical performances were found to be closely dependent on the stoichiometric compositions of the alloys. High discharge capacities approaching 500 mAh/g were achieved for the $AB_{1.95}$ alloy. At 500 mA/g current density, the discharge capacity was maintained as high as 80%, with very low capacity retention after 500 cycles. The alloy which had the highest capacity retention after 500 cycles was found to be $AB_{2.0}$ alloy. Furthermore, $AB_{2.0}$ alloy showed an excellent cyclic stability together with a high hydrogen diffusion coefficient. Studies of hydrogen diffusion coefficients showed that annealing enhanced the H diffusion rates allowing advanced performance at high discharge current densities. This has been related to a higher content of C15 Laves compound which allows to reach a higher H mobility in contrast with higher storage capacity observed for the C14 Laves type polymorph.

1. Introduction

Nickel metal hydride (Ni-MH) batteries are considered as safe and robust batteries with low manufacturing costs, high energy efficiency and environmental friendliness [1–3]. Zr-based AB_2 Laves phase type hydrogen storage alloys are promising materials as negative electrodes in metal hydride batteries that show high

* Corresponding author.
** Corresponding author. Institute for Energy Technology, Kjeller, Norway.
E-mail addresses: Ika.Dewi.Wijayanti@ife.no (I.D. Wijayanti), Volodymyr.Yartys@ife.no (V. Yartys).

storage capacities and a long cycle life [4]. On the other hand, these alloys are inferior in their activation performance, high-rate dischargeability (HRD), and cycle durability [5–7].

Laves type intermetallic compounds are used not only as anode electrodes of the metal hydride batteries but also form the largest group of hydrides used for the storage of hydrogen gas. Hexagonal C14 ($MgZn_2$ type) and cubic C15 ($MgCu_2$ type) are the most frequently used types of Laves phases which are suitable for the H storage and for the electrochemical applications. The electrochemical performance of the battery anodes when applied in the Ni-MH battery is closely related to the type of their crystal structure. C15 type alloys show an excellent HRD performance and are superior in this aspect as compared to the C14 type alloys [8,9]. However, further improvements should be achieved to advance the discharge capacity of the C15 type intermetallics, and optimization of the composition of the alloys is an important tool allowing to reach such a goal [10,11].

The stoichiometry plays an important role in designing multiphase C15 type AB_2 based alloys in order to achieve improved performance [12,13]. Variation of the stoichiometry in the C15 type AB_2 based alloys composition was found to have a very significant effect on the phase structural and electrochemical properties [14–16]. Hypo-stoichiometric Zr-based AB_{2-x} alloys with excess of the elements on the A-side and B/A ratio <2.0, were reported to show improved hydrogenation kinetics, higher hydrogen storage capacities, and lower plateau pressures than the stoichiometric and over-stoichiometric AB_{2+x} ones [17]. As an example, in Ref. [18] it has been shown that an excess of Mn in the composition of the $ZrMn_{2+x}$ alloy system with x = 0.6, 0.8, and 1.8 substantially reduced the stabilities of the hydrides and raised the equilibrium hydrogen pressures. This has been linked to the replacement of large Zr atoms (atomic radius 1.602 Å) by small Mn atoms (atomic radius 1.264 Å) in the lattice causing a significant decrease of the lattice parameters and "shrinking" of the unit cells.

Studies of the hydrogen storage capacity, equilibrium hydrogen pressure, and the stability of hydrides of the $Zr_{0.7}Ti_{0.3}MnFe$ alloy showed that they all significantly change as compared to the $Zr_{0.8}Ti_{0.2}MnFe$ alloy [19] having a higher Zr/Ti ratio. In particular, the replacement of Zr by Ti decreased the unit cell parameters which caused the reduction of the stability of the hydrides. The work [20] also showed that the hydrogen storage capacity gradually decreased when x > 1 in the $Zr_{0.9}Ti_{0.1}(Mn_{0.6}V_{0.2}Co_{0.1}Ni_{1.1})_x$ alloys. Furthermore, the increase of the stoichiometric ratio (x > 1) led to an increase of the equilibrium pressure (to the values exceeding 1 bar) creating the conditions when the reversible electrochemical capacity would be difficult to achieve. At the same time, two over-stoichiometric alloys showed a smaller hysteresis than the other alloys.

15 alloys with three different B/A element combinations with various ratios for 5 different $AB_{2\pm x}$ stoichiometries (1.8, 1.9, 2.0, 2.1, and 2.2) were studied in Ref. [21]. It has been found that the maximum capacities were obtained for the $AB_{1.9}$ alloys. For the alloys with over-stoichiometric composition (B/A > 2.0), the hydrogen storage capacities decreased.

Three hypo-stoichiometric alloys, including $Zr_{0.7}Ti_{0.3}(Mn_{0.2}V_{0.2}Cr_{0.15}Ni_{0.45})_{1.8}$, $Zr_{0.65}Ti_{0.35}(Mn_{0.3}V_{0.14}Cr_{0.11}Ni_{0.65})_{1.76}$, and $Zr(Mn_{0.2}V_{0.2}Ni_{0.6})_{1.6}$ alloys, were studied in Ref. [22]. Excellent hydrogen storage capacities were achieved, together with improved cycle life and higher electrochemical discharge capacities.

Our earlier publications related to the topic studied in the current work were focused on the effect of rapid solidification process of $Ti_{12}Zr_{21.5}V_{10}Cr_{7.5}Mn_{8.1}Co_8Ni_{32.2}Al_{0.4}Sn_{0.3}$ as C14 [23] and $Ti_{0.15}Zr_{0.85}La_{0.03}Ni_{1.2}Mn_{0.70}V_{0.12}Fe_{0.12}$ as C15 [24] predominated alloys aimed to improve the performance of the AB_2 based Laves type

alloys as battery anode materials. After the rapid solidification both alloys achieved a significant improvement in their discharge capacities and rate performances. However, the activation performance of the alloys became inferior. The worsening of the activation performances occurred for the melt-spun alloys due to the formation of the thicker oxide layers and the changes in chemical composition of the LaNi-based secondary phase which was no longer acting as a catalyser to speed up the hydrogenation during the activation.

Annealing treatment was applied to the two C15 predominated alloys including $Ti_{0.15}Zr_{0.85}La_{0.03}Ni_{1.2}Mn_{0.7}V_{0.12}Fe_{0.12}$ [25] and $Ti_{0.2}Zr_{0.8}La_xNi_{1.2}Mn_{0.7}V_{0.12}Fe_{0.12}$ (x = 0.01–0.05) [26] and resulted in achieving excellent discharge capacity performance including high reversible storage capacity, together with easy activation, fast kinetics of charge, and low hysteresis observed in the isotherms of hydrogen absorption-desorption. Both alloys achieved high discharge capacities, 410 mAh/g and 420 mAh/g, respectively. 3 wt% of La was added to both alloys causing an easier activation and an increased capacity.

However, the improvements of the performance for the anode materials are still in need aimed to achieve higher discharge capacities and better rate performances.

In the present study, to satisfy the demands for developing the advanced Ni-MH battery with improved performance and enhanced hydrogen storage capacity, the alloys with the hypo-stoichiometric Laves type composition $AB_{2-x}La_{0.03}$ (A = $Ti_{0.15}Zr_{0.85}$; B=$Mn_{0.64–0.69}V_{0.11–0.119}Fe_{0.11–0.119}Ni_{1.097–1.184}$; x = 0, 0.05 and 0.1) were prepared by arc melting and annealing. Our goal was to study the effect of changing the ratio between A (Ti, Zr) and B (Mn, V, Fe, Ni) components in the annealed alloys including their phase-structural composition and microstructure, gaseous hydrogen absorption-desorption and electrochemical properties, together with Alternating Current (AC) impedance characterization to probe the rates of hydrogen diffusion in the alloys.

2. Experimental methods

Approximately 10 g alloys with the composition of $AB_{2-x}La_{0.03}$ (A = $Ti_{0.15}Zr_{0.85}$; B=$Mn_{0.64–0.69}V_{0.11–0.119}Fe_{0.11–0.119}Ni_{1.097–1.184}$; x = 0, 0.05 and 0.1) (see Table 1) were prepared by arc melting on a water-cooled copper hearth under argon atmosphere and re-melted three times to improve their homogeneity. The purity of each element constituent was not less than 99.7%. The variation of chemical composition of the alloys for the B components (transition metals) was intended at the preparation of the hypo-stoichiometric compositions $AB_{1.9}$, $AB_{1.95}$, and $AB_{2.0}$ (see Table 1). In order to compensate for the partial evaporation at high melting temperatures, 3 wt% of excess of Mn was added to the mixture of the components prepared for the arc melting preparation as compared to the aimed stoichiometric composition.

After the melting, the as-cast alloy ingots were sealed into stainless-steel tube sample holders filled with Ar and then transferred into an annealing furnace. These alloys were then annealed at 950 °C for 24 h and then quenched into cold water (4 °C) resulting in their homogenization.

Table 1
Chemical composition of the annealed alloys $AB_{2-x}La_{0.03}$ (in atoms/$AB_{2-x}La_{0.03}$).

Alloys	Ti	Zr	La	Ni	Mn	V	Fe	B/A
$AB_{1.9}$	0.15	0.85	0.03	1.097	0.64	0.11	0.11	1.90
$AB_{1.95}$	0.15	0.85	0.03	1.126	0.657	0.113	0.113	1.95
$AB_{2.0}$	0.15	0.85	0.03	1.155	0.674	0.116	0.116	2.0

The annealed alloys were characterized using the following techniques:

2.1. Structural characterization

XRD measurements were performed on the powders of less than 40 μm in size by using a monochromator-equipped Bruker D8 diffractometer ($\lambda = 1.5418$ Å (CuK$_{\alpha 1}$), step-size: 0.01975° 2θ, Bragg-Brentano geometry), with a 2 theta measurements range of 10°−120°. The experimental data was processed using Rietveld refinements and GSAS software [27]. A HITACHI FlexSEM 1000 VP-SEM equipped with EDS analysis was used to study the microstructures, distribution of phases, and the local composition of the phases in the samples.

2.2. Characterization of alloys interaction with hydrogen using alloy-H$_2$ gas and electrochemical techniques

The powdered samples, about 0.5−1 g in mass, were inserted into a stainless-steel sample cell placed into a thermostated autoclave and activated in vacuum at 250 °C for 30 min. The hydrogen absorption-desorption isotherms were measured at 20, 50 and 80 °C (293, 323 and 353 K), after a completion of the alloy's activation. Several hydrogen absorption-desorption cycles were performed before measuring equilibrium P−C−T diagrams.

The powders of 40−60 μm were mixed with carbonyl Ni powder in a weight ratio of 1:4, respectively. The mixture (appr. mass 500 mg) was then cold-pressed under a 12 MPa pressure to prepare the pellets with a diameter of 10 mm. The final step to make the anodes was to place the pellet in between two Ni foams and to prepare a compacted sandwich type electrode. Electrochemical performance was characterized using a CT 2001 Land Battery Tester and three-electrode system measurements.

2.3. EIS characterization

Electrochemical Impedance Spectroscopy (EIS) characterization was performed using SP-300-Potentiostat from Bio-Logic Science Instruments. Galvanostatic Electrochemical Impedance Spectroscopy (GEIS) technique was applied by performing the measurements at 0.1 kHz−0.5 mHz frequencies with the 10-mA current amplitude. Hydrogen diffusion coefficients in the electrodes were calculated using Fick's equation, for more details please consult our earlier publication [24].

2.4. Studies of the metal - hydrogen gas interactions

The experimental study of metal - hydrogen gas interaction was carried out using in-house made Sieverts-type installation, in the range of temperatures 20−80 °C at hydrogen pressures from 0.1 to 25 bar absolute. The accuracy of the measurements was ±0.02 bar for H$_2$ pressure and ±0.3 Ncm^3/g for the hydrogen concentration in the solid.

The PCT data was further processed by:

(a) Plotting experimental data in van't Hoff coordinates Ln(P$_{eq}$) versus 1/T to yield apparent values for the entropy (ΔS) and entropy (ΔH) changes during hydrogenation and dehydrogenation. The experimental values of the equilibrium pressures, P$_{eq}$, were taken for the plateau midpoint at hydrogen concentration, C$_H$, of 0.7 wt %, separately for H absorption and desorption.

(b) Fitting of the whole PCT datasets using a semi-empirical model of phase equilibria in the metal - hydrogen systems [30]. The fitting of the experimental data allowed to further

refine the ΔS and ΔH values for the desorption (commonly considered as representing a "true" equilibrium), as well as to further analyze PCT diagrams to derive maximum H storage capacity, critical temperature, hysteresis energy loss, plateau slope (see Supplementary information for the details).

3. Results and discussion

3.1. Phase-structural characterization by XRD

Measured XRD patterns and Rietveld refinements of the XRD data for three studied alloys are shown in Fig. 1 and in a Supplementary Information file (Figure S1, a and b). The annealing improved the homogeneity of the alloys, as compared with the as cast alloys. The refinements showed that C15 phase is a predominant constituent (>95 wt %) in all studied annealed alloys. Further to the main cubic C15 phase the homogenized alloys also contained two secondary phases, a C14 Laves phase intermetallic and a LaNi intermetallic compound.

The crystallographic data and abundances of the phase constituents are listed in Table 2.

Refinements of the XRD data show that the experimental and calculated pattern well agree with each other. AB$_{1.95}$ alloy has the highest abundance of C15 phase (98.3 wt%), followed by AB$_{2.0}$ (97.2 wt%), and AB$_{1.9}$ (95.2 wt%). In turn, AB$_{1.9}$ alloy has the highest abundance of C14 phase (4.6 wt%), followed by AB$_{2.0}$ (2.7 wt%), and AB$_{1.95}$ (1.5 wt%). For LaNi phase, its abundance is small, 0.8 wt% in maximum for the AB$_{1.95}$ alloy. Nevertheless, despite of the small abundance, LaNi phase has an important role in the activation of the hydrogenation process by the alloys.

From Table 2 we conclude that:

(a) The XRD refined crystal structure data for the annealed alloys well agree with the results of our previous publications [25,26]. With increasing B/A stoichiometry in the alloys, the lattice constants and the unit cell volumes decrease. The atomic radii of the A site elements are normally larger than that for the B elements. With increasing B/A stoichiometry, the excessive elements in B site occupy A sites which causes shrinking of the unit cells [28].

(b) The alloy with higher content of Ti [26] shows the smallest unit cell volume of C15 phase as compared to the results of the present study and previous alloy with less content of Ti. The substitution of Zr atoms (1.602 Å) by Ti atoms which have the smaller radii (1.462 Å) caused shrinkage of unit cells [29].

(c) When changing the stoichiometry (from AB$_{1.9}$ to AB$_{2.08}$), the abundance of C15 phase increases and the abundance of the C14 phase decreases. Thus, increasing the B/A stoichiometric ratio causes a better homogeneity of the alloys.

3.2. Microstructural analysis

Microstructures of as-cast and annealed AB$_{1.95}$ alloys characterized using SEM in a back-scattered electron (BSE) mode and are presented in Fig. 2 as a typical example.

The microstructure of the as cast alloy shows presence of three phase constituents which based on the data of the XRD study were identified as a C15 type matrix phase (dark grey grains in Fig. 2a) and two minor in abundances phase constituents, including a light grain C14 phase formed in between the grain boundaries of the C15 intermetallic, and a white globular grains of the LaNi intermetallic.

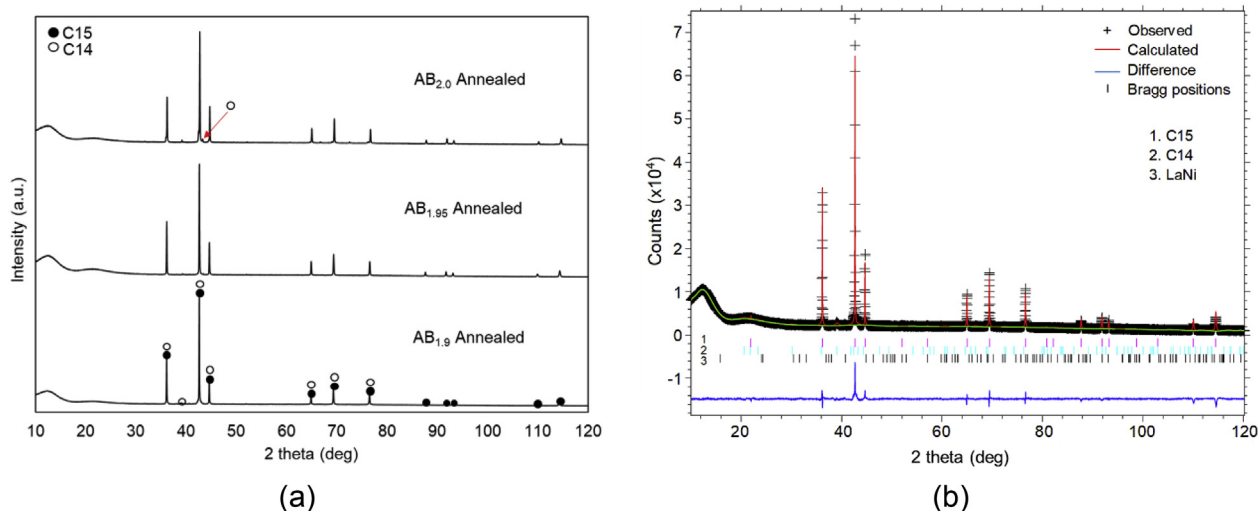Annealing of the alloy resulted in its homogenization

Fig. 1. XRD patterns (Cu-K$_{\alpha 1}$) for the studied alloys (a) and typical Rietveld refinement for the AB$_{1.9}$ annealed alloy shown as an example (b). Two Laves phase type intermetallics (C15 and C14) are present. Content of C15 phase exceeds 95 wt % for all studied alloys, see Table 1.

manifested by a decreased content of the C14 phase in the annealed alloy, as is clearly seen from a comparison of the micrographs shown in Fig. 2a–d. The annealing also results in a growth of the size of the LaNi grains as is clearly seen from a comparison of the Fig. 2a and c.

Table S1 shows that the annealing leading to the homogenization of the alloy does not change the overall stoichiometry of the alloy which remains very close to the composition of the as-cast alloy.

3.3. Hydrogenation properties of the AB$_{1.90}$, AB$_{1.95}$ and AB$_{2.0}$ alloys

After the activation by heating in vacuum for 30 min at 300 °C all studied AB$_{1.90}$, AB$_{1.95}$ and AB$_{2.0}$ alloys show a fast kinetics of hydrogen absorption and in just a few minutes form saturated hydrides when hydrogenated at hydrogen pressure of 20 bar H$_2$. After the synthesis of the saturated hydrides these hydrides of the AB$_{2-x}$ alloys with stoichiometric B/A ratios of 1.90, 1.95 and 2.0 were used to study Pressure-Composition-Temperature (PCT) isotherms

of hydrogen absorption and desorption. Studies of the PCT shown in Fig. 3 were performed at 20, 50, and 80 °C.

Increase in B/A leads to a decrease in the H storage capacity, from appr. 1.72–1.75 wt % H for AB$_{1.9}$ and AB$_{1.95}$ alloys to 1.55 wt% for the AB$_{2.0}$-based hydride. Increasing the temperature of the P–C measurements leads to the narrowing of the plateau range for of each of the studied alloys indicating increased homogeneity range for both α-solid solution and for the β-hydride phase. It is easy to note that the hysteresis between the hydrogen absorption and desorption plateau decreases with increasing temperature of the measurements and is the smallest at 80 °C. This indicates that the critical temperature of the studied metal-hydrogen systems should be slightly above 80 °C.

By using van't Hoff equation and PCT modelling approach [30], the thermodynamic parameters of the hydride formation-decomposition were obtained. These parameters for the AB$_{2-x}$-based hydrides are listed in Table 3. As can be seen from the Table 3, AB$_{1.9}$ alloy has the lowest ΔH and ΔS formation of 33.98 kJ/mol H$_2$ and 107.67 J/mol H$_2$ followed by the AB$_{1.95}$ and AB$_{2.0}$ alloys. The

Table 2
Crystallographic data and phase abundances for the annealed AB$_{2-x}$La$_{0.03}$ Laves type alloys from the Rietveld GSAS refinements.

Alloys	Phase	Space group	Unit cell parameters, Å				Abundance (wt.%)
			a	b	c	V, Å³	
AB$_{1.9}$	C15	$Fd\overline{3}m$	7.0374(6)	–	–	348.532(1)	95.2(1)
	C14	$P6_3/mmc$	4.9969(1)	–	8.1817(5)	176.920 (1)	4.3(1)
	LaNi[a]	$Cmcm$	3.902(7)	10.78(2)	4.385(8)	184.449(6)	0.5(6)
AB$_{1.95}$	C15	$Fd\overline{3}m$	7.0338(6)	–	–	348.004(9)	98.3(4)
	C14	$P6_3/mmc$	4.9834(4)	–	8.1053(1)	174.325(2)	0.9(1)
	LaNi	$Cmcm$	3.902(7)	10.78(2)	4.385(8)	184.449(6)	0.8(5)
AB$_{2.0}$	C15	$Fd\overline{3}m$	7.0235(7)	–	–	346.468(1)	97.2(1)
	C14	$P6_3/mmc$	4.9941(3)	–	8.1533(8)	176.111(2)	2.7(7)
	LaNi	$Cmcm$	3.902(7)	10.78(2)	4.385(8)	184.449(6)	0.1(5)
Reference data for Ti$_{0.15}$Zr$_{0.85}$La$_{0.03}$Ni$_{1.2}$Mn$_{0.7}$V$_{0.12}$Fe$_{0.12}$ alloy [25]							
AB$_{2.08}$	C15	$\boldsymbol{Fd\overline{3}m}$	7.0235(1)	–	–	346.466(1)	99.1(1)
	LaNi	$Cmcm$	3.902(7)	10.78(2)	4.385(8)	184.449(6)	0.9(1)
Reference data for Ti$_{0.2}$Zr$_{0.8}$La$_{0.03}$Ni$_{1.2}$Mn$_{0.7}$V$_{0.12}$Fe$_{0.12}$ alloy [26]							
AB$_{2.08}$	C15	$\boldsymbol{Fd\overline{3}m}$	7.0163(1)	–	–	345.41(1)	100

[a] Rietveld refinements of LaNi phase were performed by using the reference data from Ref. [25].
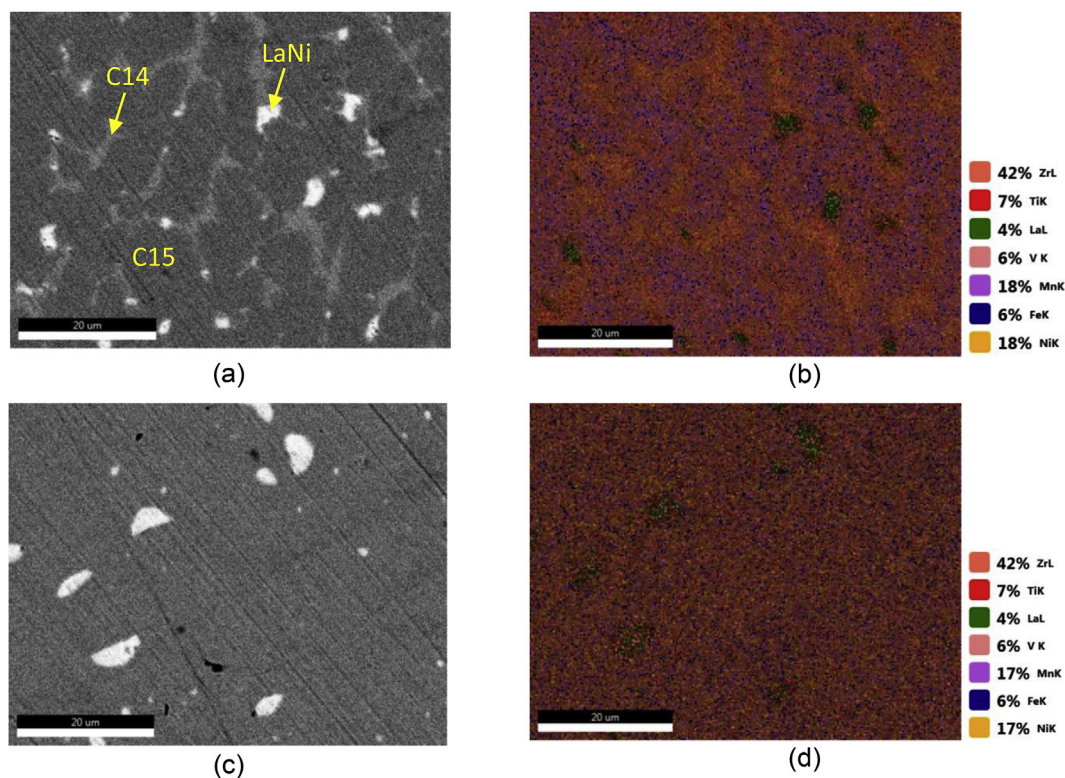
Fig. 2. SEM images of AB$_{1.95}$ as-cast (a) and its elemental mapping (b), annealed (c) and its elemental mapping (d). Different color on the images indicates different element composition. (For interpretation of the references to color in this figure legend, the reader is referred to the Web version of this article.)

data presented in Table 3 are in good agreement with our earlier publication on the properties of the hydride of the AB$_{2.08}$ alloy [25].

In addition to Table 3, we can see that the critical temperatures have rather low values, around 100 °C, with a trend of decrease in their values following an increase in B/A ratio and the lowest value of 366 K (93 °C) observed for AB$_{2.0}$ alloy.

3.4. PCT modelling results

The experimental PCT data (both H$_2$ absorption and desorption in one dataset) were fitted by the developed by the authors semi-empirical model [30] assuming that the metal hydride formed is described by a core model of van der Waals lattice gas with one plateau segment present at the Pressure-Composition isotherms.

All model parameters except of slope factors (fixed values were used) were refined. Refinement of the slope factors which has the range between 0 and 0.1 was required only in the cases when the isotherms showed a combination of flat plateaux and smooth transitions from the α- and β-solid solution regions into two-phase (α+β) region.

As can be seen from the results presented in Supplementary Material (Tables S3–S5), in all cases the fitting was reasonably good, with the goodness of fit R-factors below 0.15% for AB$_{2.0}$ and below 0.3% for the alloys with B/A < 2.0.

According to the modelling procedure [30], the accuracies of the refinements of the fitting parameters (values in brackets in Table 3; column "Error" in Table S4) were estimated as their variances which resulted in the increase of the total squared deviation of the experimental points from the calculated isotherms by 1%.

From Fig. 3 (f) and Tables S3–S5 we can conclude that enthalpy of formation remains practically unchanged, -(34–35) kJ/mol H$_2$ and is independent of the composition for the AB$_{1.90}$, AB$_{1.95}$ and AB$_{2.0}$ alloys. Thus, an obvious decrease in the stability of the

hydrides manifested by a significant increase of equilibrium dissociation pressure, from 0.4 to 0.85 bar H$_2$, is caused by the changes in entropy of phase transformation, from −108 to − 118 J/(mol H$_2$ K).

All the alloys are characterized by rather low (below 366−386 K) critical temperatures of α−β transformation (T$_C$; minimum value was observed for the stoichiometric alloy) and low (below 1 kJ/mol) hysteresis energy losses (ΔG$_h$). At the same time (see Fig. 3 (g)), the increase of B/A from 1.9 to 2.0 results in a doubling of ΔG$_h$ and a significant increase of hysteresis.

The pressure − composition isotherms for all the alloys were characterized by moderately sloping plateaux (distribution width parameter shows width of hydrogen absorption-desorption plateau, w~0.15 which is obtained by PCT modelling, see Tables S3−S5) but quite high contributions of Lorentz profile shows the shape profile of the plateau PCT, η (which is obtained by PCT modelling, in most cases, higher than 0.5, see Tables S3−S5) that indicates a low PCI curvatures in the transient regions between plateau and α- or β-solid solutions. As it was noted in Ref. [31], such a feature (sloping of P(C) dependence at the initial and final stages of hydride formation/decomposition) is associated with stress effects accompanying the hydride phase formation.

3.5. Electrochemical characterization

The activation performances of studied alloys at 100 mA/g current density are shown in Fig. 4 (a). As mentioned earlier, the aim of adding Lanthanum was to improve the activation performance of the alloys. 3 wt% La is the optimized and effective amount resulting in the most efficient activation of the Zr based AB$_2$ alloys. This is in agreement with our earlier publications [25,26]. Indeed, the alloys studied our earlier publications which were activated in the fourth cycle with a maximum capacity of 370 mAh/g [25] and 360 mAh/g
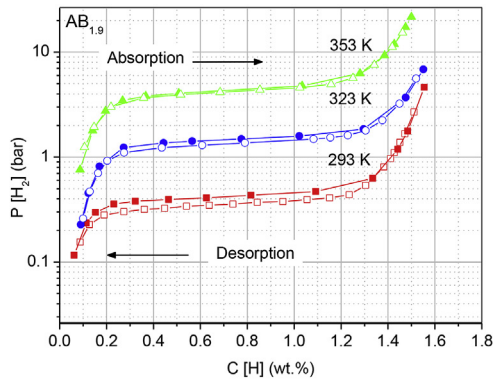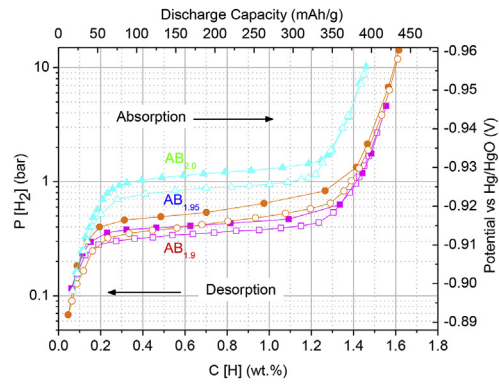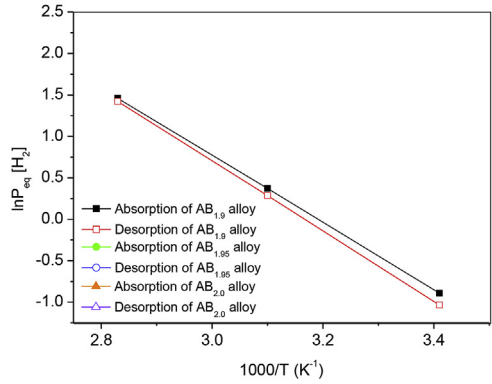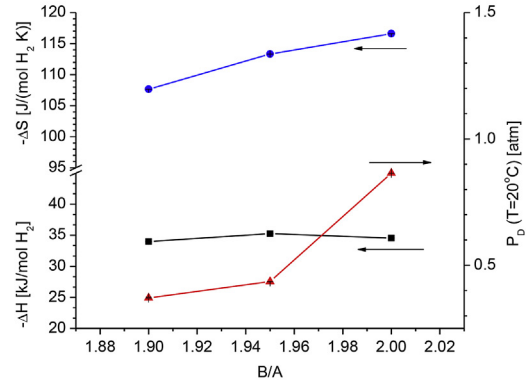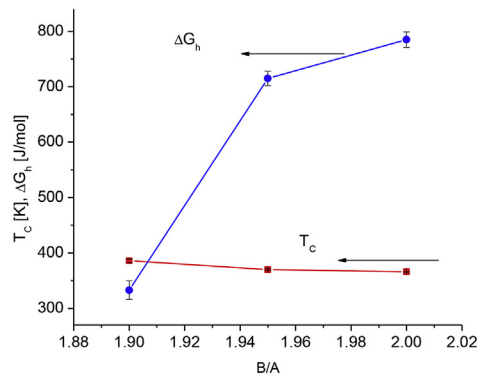
(a)
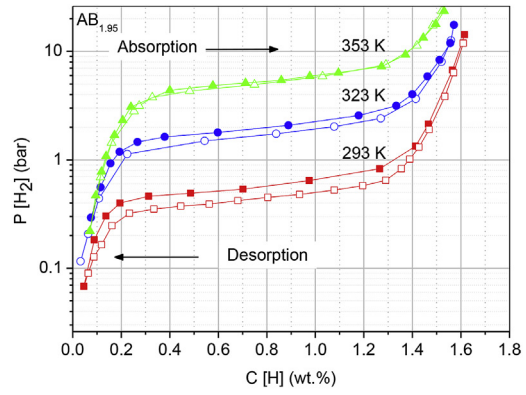
(b)
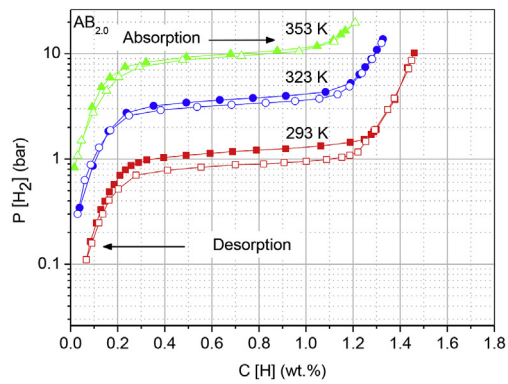
(c)

(d)

(e)

(f)

(g)

Table 3
Thermodynamic properties of AB_x hydrides (taken from the PCT modelling data).

Samples	Fitting parameters					Calculated H content (P = 100 bar, T = 298 K)	
	Plateau parameters (H_2 desorption)		Hysteresis energy loss	Critical temperature	Asymptotic H concentration		
	$-\Delta H$, kJ/mol H_2	$-\Delta S$, J/mol H_2 K	ΔG_{h}, J/mol H_2	T_C, K	C_{max}, Ncm^3/g wt.% H	C_H, Ncm^3/g wt.% H	C_H, mAh/g
$AB_{1.9}$ (annealed)	33.98(2)	107.67(1)	333(17)	386(3)	231.1(6) 2.077	192 1.725	462.3
$AB_{1.95}$ (annealed)	35.25(1)	113.33(3)	715(13)	370(1)	236(2) 2.121	195 1.753	469.8
$AB_{2.0}$ (annealed)	34.54(1)	116.61(1)	785(14)	366(1)	210.9(5) 1.896	173 1.555	416.8

[26], while the presently studied hypo-stoichiometric alloys became activated in the fifth cycle with maximum capacity of 390 mAh/g reached for the $AB_{1.95}$ alloy. $AB_{2.0}$ alloy shows a slightly lower activation capacity, 370 mAh/g.

Fig. 4 (b) presents discharge capacity of $AB_{1.90}$, $AB_{1.95}$, and $AB_{2.0}$ alloys performed at 100 mA/g current density. As can be seen, all studied alloys show close values of the plateaux of discharge potentials, which became longer, flatter, and were located between −0.875 and −0.915 V $AB_{1.95}$ shows the longest and flattest plateau of discharge potentials and the best performance among the studied alloys.

As shown in Fig. 4 (d), $AB_{1.95}$ alloy achieved the best HRD performance among the other alloys by showing the smallest decrease in the discharge capacity at increasing current densities (see Fig. 4 (c) and (e)).

HRD performance can be characterized as the ratio between the capacities shown at the highest current density of 500 mA/g as compared to the capacity at the lowest current density of 10 mA/g. The $AB_{1.9}$ alloy with the largest unit cell showed the best discharge capacity as shown in Fig. 4 (d).

Cyclic performance of the alloys studied at charge-discharge current density of 300 mA/g is shown in Fig. 4 (g). With increasing the number of cycles, we observe that the alloys show a decreased linear slope. Indeed $AB_{2.0}$ alloy shows the best capacity retention among other alloys, followed by $AB_{1.9}$, and $AB_{1.95}$ alloy. The better mechanical stability in $AB_{2.0}$ alloy causes its smaller surface area thus further pulverization can be hindered resulting in its better cyclic stability [20]. Further to this, the higher content of Ni in $AB_{2.0}$ contributed to lower a corrosion rate of the alloy which resulted in the best capacity retention during the cycling.

With changing the stoichiometry of the alloy to $AB_{2.08}$ [25,26], the capacity retention shows even higher values than that for the $AB_{2.0}$ stoichiometry alloy. This is caused by a decreased pulverization due to a better mechanical stability during the cycling of the hyper-stoichiometric alloys.

3.6. H storage capacity during studies of the metal-gas interactions vs. electrochemical performance

Even though hydrogen storage capacity of the metal hydride forming alloy should provide converging data, however differences normally are observed since PCT diagrams are measured in equilibrium conditions while electrochemical characteristics are obtained dynamically during discharge in the open cells. Thus, many features can diverge, including (a) H storage capacity; (b) slope of the PCT curves or slope of the capacity-voltage dependence; (c) hysteresis or overpotential; (d) homogeneity ranges for the α-solid solution and β-hydride phase.

Thus, it is interesting to compare the data of the metal-gas interactions vs. electrochemical performance as related to the chemical composition/ratio between B and A components in the $AB_{1.90}$, $AB_{1.95}$ and $AB_{2.0}$ alloys.

Fig. 5 and Fig. S3 show the gaseous H capacity vs. electrochemical capacity of the anode electrode for the studied $AB_{2.0}$ alloy. The data in Fig. S3 also show a similar comparison for $AB_{1.9}$ and $AB_{1.95}$ alloys. Gaseous capacity is smaller than the electrochemical capacity indicating that metal hydride reaches a deeper saturation during the electrochemical environment. Furthermore, we note that the plateau of gaseous H capacity in the PCT diagrams is shorter and flatter than in for the voltage plateau of electrochemical capacity plot. $AB_{1.9}$ alloy showed the best agreement between the experimentally measured gaseous and electrochemical capacities probably because it forms the most stable hydride ($P_{eq}.H_2$ is 0.3 bar @ 293 K) thus preventing uncontrollable loss of hydrogen gas because of the desorption from the anode electrode during the electrochemical experiments in an open cell.

The hysteresis of hydrogen absorption-desorption/overpotential for the electrochemical charge-discharge process for the studied alloys shows a clear trend with increasing B/A stoichiometric ratio. The smallest hysteresis was observed for the alloy with the lowest B content, $AB_{1.9}$. However, for the alloys with B content higher than 1.9 the hysteresis increases and becomes independent of the B/A ratio. This finding is in agreement with the results of our earlier publication [25] for the hyper-stoichiometric $AB_{2.08}$ alloy, which shows a similar hysteresis with the presently studied $AB_{1.95}$ and $AB_{2.0}$ alloys.

Furthermore, the changes in the plateaux of electrode potentials show similar trends as variations of ΔG for the studied hydrides. Indeed, the changes in discharge potential, −0.9385 V for $AB_{1.9}$, −0.9505 V for $AB_{1.95}$, and −0.9652 V for $AB_{2.0}$ (middle points of the plateaux in each case), correlate with the changes in ΔG, $AB_{1.9}$: 333; $AB_{1.95}$: 715: $AB_{2.0}$: 785 J/(mol H_2) showing an interrelation between the values of the overpotential and hysteresis following an increase in the B/A ratio.

When comparing interrelation between the gaseous and electrochemical H storage capacity, one should account that the open-to-air configuration might cause loss of hydrogen from the formed hydride during the electrochemical process leading to the smaller H content in the studied metal hydride. On the other hand, it is well known that electrochemical charging can cause an opposite

Fig. 3. PCT isotherms of hydrogen absorption and desorption for $AB_{1.9}$ (a), $AB_{1.95}$ (b), $AB_{2.0}$ (c) alloys, gaseous H_2 vs. electrochemical capacity of the studied alloys at 293 K (d), van't Hoff plots showing dependence of equilibrium pressure (ln P_{eq}) of hydrogen absorption and desorption based on the PCT diagrams measured at 293, 323 and 353 K from 1/T, (e), dependencies of changes in hydrogenation entropy and enthalpy (left Y-axes) and desorption plateau pressures at T = 20 °C (right Y-axis) (f), and dependencies of hysteresis energy loss and critical temperature of α−β transformation on the stoichiometry of the $AB_{2-x}La_{0.03}$ alloys (g). The plateau pressure for absorption is shown by filled symbols while open symbols are used for the desorption in each data set.
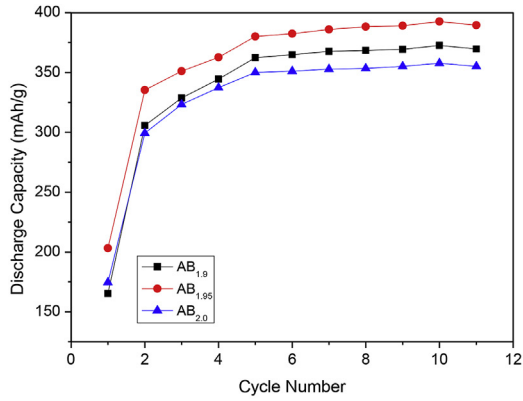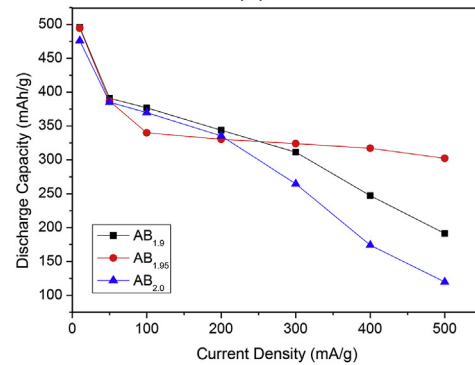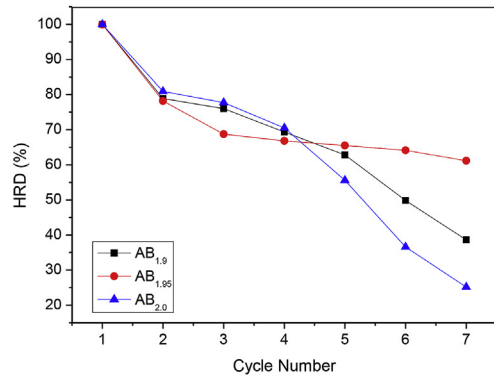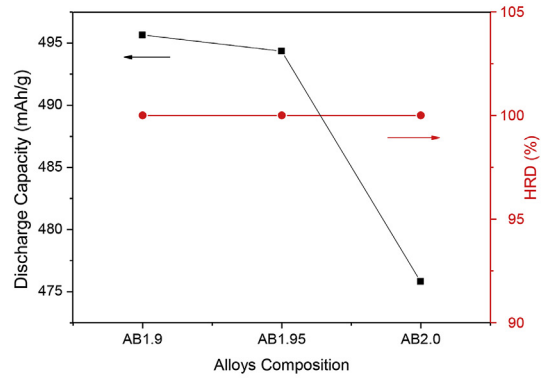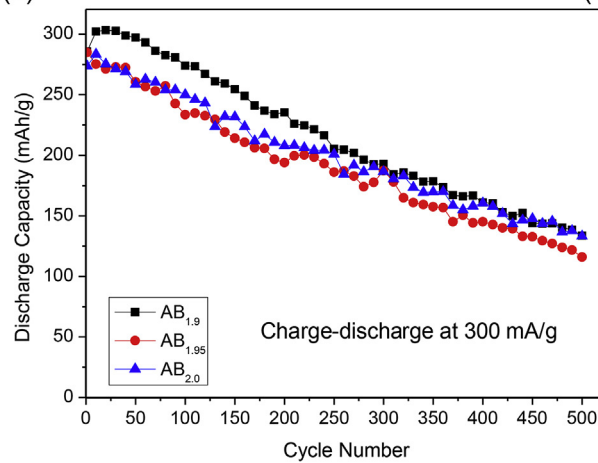
(a)
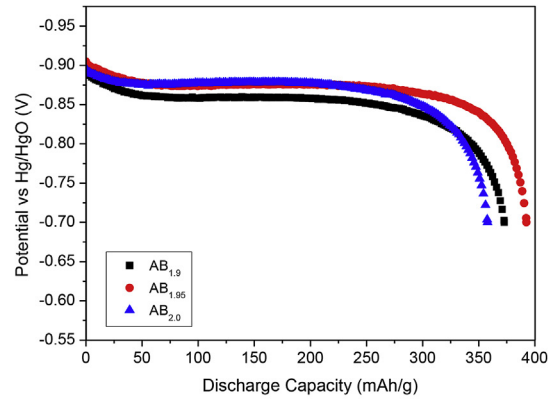
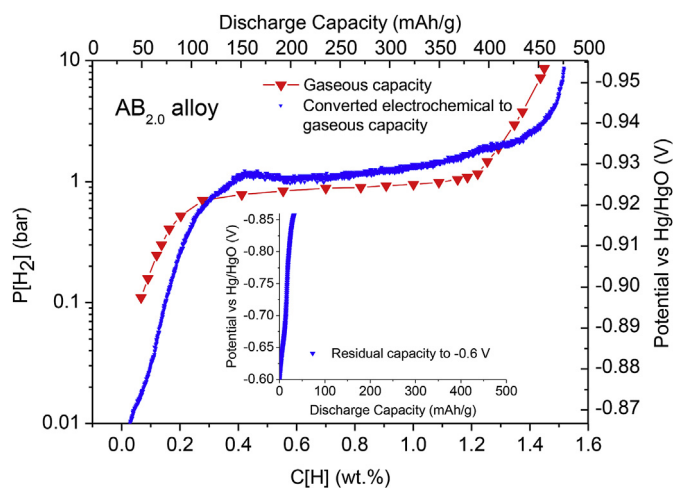(b)
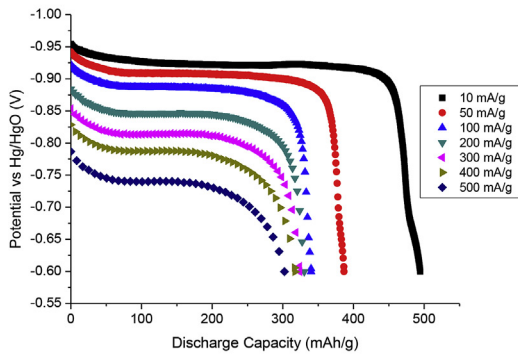
(c)

(d)

(e)

(f)

(g)

Fig. 5. Gaseous capacity vs. electrochemical capacity for $AB_{2.0}$ alloy. The inserts of the graphs show the tails of the curves measured from -0.85 to -0.6 V (cut-off voltage applied during the measurements of the discharge electrochemical capacity).

behaviour when electrochemical charging allows even at ambient conditions using a promotor of the hydrogenation to synthesize hydrides requiring application of high pressures of hydrogen gas (example: Ni hydride NiH which has been synthesized electrochemically [32] while in the nickel-hydrogen system equilibrium pressure of hydrogen desorption was measured as being around 4 kBar H_2 at room temperature [33]. Thus, measurements in the close electrochemical cells allowing to control H_2 pressure and to use overpressures could be valuable in the future work.

3.7. EIS studies

EIS characterization was performed for the studied alloys to assess characteristics of hydrogen diffusion. 50% State of Charge (SoC) samples were used to measure the EIS spectra after performing different number of cycles, 10, 100, 200, 300, 400, and 500.

EIS spectra of the studied alloy electrodes at 50% SoC and different number of performed cycles are shown at Fig. S4. We note that all the alloys show an unusual depressed semicircles shape of EIS spectra. Such a behaviour was also observed in our earlier study [25], were we used an equivalent circuit containing the Constant Phase Element (CPE) instead of a commonly used capacitance. Surface inhomogeneity/surface roughness is expected to cause such an uncommon shape of the EIS spectra. Therefore, in order to achieve a better fit of the EIS data, CPE was used to replace capacitance to properly describe the depressed semicircle shape of Nyquist plot. In addition to the equivalent circuit, a series of modified Randles circuits with added CPE and parallel circuit elements consisting of R and CPE was applied to fit the EIS spectra to achieve more accurate fitting results (Fig. 6 (a)).

As shown in Fig. S4, the alloys show a similar shape of the EIS spectra for the cycled sample by containing a Warburg element in the low frequency region related to the hydrogen transport in the studied alloys. It appears that the slope and the length of Warburg elements are different for each measurement. For longer cycled samples, the contact resistances, charge transfer resistances, and Warburg elements were all decreased, showing that the cycling performance generally results in a better hydrogen transport in the
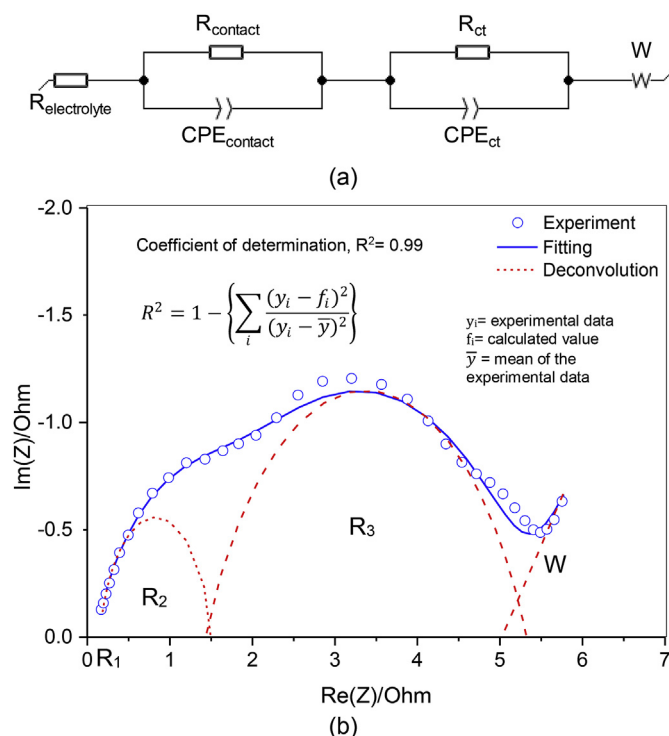

Fig. 6. Modified equivalent circuit used to fit the EIS experimental data (a), and deconvolution of Nyquist impedance plot for 50% SoC of $AB_{1.9}$ annealed alloy achieved by using a superposition of equivalent circuits, where $R_1 = R_{electrolyte}$, $R_2 = R_{contact}$, $R_3 = R_{ct}$, and W = Warburg element (b). Successful deconvolution result was shown by the coefficient of determination (R^2) value of 0.99, or close to 1.

electrodes.

The EIS spectra resulted from the measurements were fitted by using the modified equivalent circuit shown in Fig. 6 (a) - to determine the values of parameters in equivalent circuit. Further to the fitting, the deconvolution has also been done by configuring and by superimposing two semicircles and a straight-line dependence to represent the equivalent circuit model. The EIS parameters values resulting from the deconvolution (see Fig. 6 (b)) were then compared with the results from the fitting. 8 different parameters describing the physical properties of the studied alloy electrodes were obtained by the fitting, including $R_{electrolyte}$, $R_{contact}$, $CPE_{contact}$, n_1, $R_{charge\ transfer}$, $CPE_{charge\ transfer}$, n_2, and σ. The values of these parameters for the studied alloys as related to the number of the applied cycles are shown in Tables S6–S12. Further to these results, in order to determine the quality of the fit and deconvolution, the Goodness of fit (χ^2) and Coefficient of determination (R^2) values were used. As the values for χ^2 obtained from the EIS spectra fitting were less than 0.9, this indicated that the applied equivalent circuit model produces an excellent fitting. Thus, suggested deconvolution resulted in the excellent agreement with experimental data as R^2 values were close to 1.

To summarize, the EIS spectra for each studied alloy at 50% SoC and subjected to a different number of cycles were shown in Fig. S4. After the activation, all alloys show a larger total resistance, while after 500 cycles the results show that the total resistance decreased. We also can see that the length and the angle of Warburg impedance decreased during the cycling which means the that the

Fig. 4. Activation performance (a); discharge capacity (b) for the studied alloys at 100 mA/g current density; the capacity of the studied alloys at variable discharge current densities and cut-off potentials (c); rate performance (d); HRD performances (e); comparison of the performance of the studied samples as related to composition of the studied alloys (f); cycling performances of studied alloys measured at 300 mA/g with the capacity retention of $AB_{1.9}$ = 46.7%, $AB_{1.95}$ = 40.7%, and $AB_{2.0}$ = 48.7% (g).
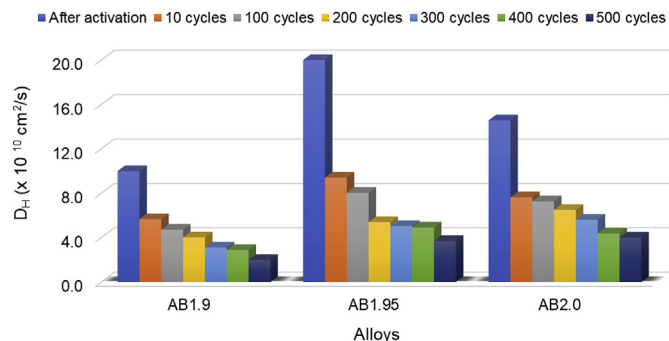
Fig. 7. Hydrogen diffusion coefficient (D_H) for the studied alloys as related to the cycles number at 50% SoC. The smallest decrease of hydrogen diffusion coefficient vs. cycle number is observed for $AB_{2.0}$ alloy.

hydrogen diffusion was significantly facilitated by the cycling. Probably this can be associated with a gradual cracking of the alloy powder particles resulting in a faster charge and discharge of the smaller particles.

We observe that the contact resistance of the studied alloy electrodes decreased with repeated cycling indicating that corrosion of the alloys surface has not been extensive and did not produce the oxide/hydroxide layer on the surface, while the reduction of the resistance could be related to a gradual decrease of the particle size during expansion and contraction followed by the cracking taking place during the cycling of hydrogen uptake and release.

Fig. 7 shows the hydrogen diffusion coefficient (D_H) for the studied alloys as related to the number of applied cycles for the electrodes with 50% SoC. We observed a large difference between the hydrogen diffusion coefficient value after activation and during the cycling. After activation, $AB_{1.95}$ shows the largest hydrogen diffusion coefficient which is almost 2×10^{-9} cm^2/s, followed by $AB_{2.0}$ 1.5×10^{-9} cm^2/s and $AB_{1.9}$ alloys 1.0×10^{-9} cm^2/s. Furthermore, we note that stoichiometric $AB_{2.0}$ alloy shows an excellent cyclic stability and shows a fast H diffusion even after 500 cycles (see Fig. 7).

4. Discussion

PCT isotherms of hydrogen absorption and desorption for all studied alloys were measured at 20, 50, and 80 °C. These isotherms are presented in Fig. 3 and show that they all form stable at ambient conditions hydrides with dissociation pressures 0.4–0.8 bar H_2. Increasing B/A results in a gradual decrease in the H storage capacity. Fitting of the PCT data for the studied alloys shows that for the hypo-stoichiometric alloys their H storage capacity is around 2.1 wt % H, while the capacity drops to 1.9 wt% H for the hydride formed by a stoichiometric $AB_{2.00}$ alloy. Indeed, $AB_{1.95}$ alloy has the highest capacity among other alloys with the similar Zr-based AB_2 Laves phase alloys, which are $Zr_{0.9}Ti_{0.1}V_{1.9}$ alloy with the capacity 1.1 wt% of hydrogen [17], $ZrMn_{2.8}$ and $ZrMn_{3.8}$ alloys with the capacity 1.44 and 1.14 wt% of hydrogen respectively [18], and $AB_{1.9}$ produced by Young with having capacity of 1.4 wt% of hydrogen [21]. This concludes that the studied alloy shows an excellent hydrogen storage capacity.

Increasing temperature leads to a narrowing down the plateaux indicating that the H capacity is the highest at room temperature. Interestingly, the hysteresis at higher temperatures becomes smaller confirming that the loss in the efficiency of the material due to its deformation during absorption-desorption of hydrogen becomes less pronounced at higher temperatures. In addition to this,

plateaux become narrower, and equilibrium pressures increase (see Fig. 3 (d)). It appears that the hysteresis in the alloy hydrides shows an opposite trend with increasing stoichiometry. The smallest hysteresis was observed for the alloy with the lowest B/A stoichiometry, $AB_{1.9}$. However, the alloys with a higher than 1.9 B/A stoichiometry show a similar behaviour concluding that varying the stoichiometry in Ti–Zr AB_2 based Laves alloys has a modest effect on the hysteresis. Indeed hyper-stoichiometric $AB_{2.08}$ alloy studied in our previous work [25] got a similar value of hysteresis as presently studied $AB_{1.95}$ and $AB_{2.0}$ alloys.

Using van't Hoff relation and a modelling approach [30], the thermodynamic parameters of the interaction in the studied systems were obtained and these are listed in Table 3. We can see in the Table 3, $AB_{1.9}$ alloy has the lowest ΔH and ΔS formation 33.98 kJ/mol H_2 and 107.67 J/mol H_2 which are in good agreement with our previous publication $AB_{2.08}$ alloy [25], followed by $AB_{2.0}$, and $AB_{1.95}$ alloys. From the Table 3, enthalpy of desorption has similar values for all studied hydrides, being a range 34.0–35.3 kJ/mol H_2. However, significant differences in the stabilities of the hydrides were observed with equilibrium pressure of H_2 desorption @ 293 K changing from 0.4 to 0.85 bar H_2 following increase in B/A ratio from 1.90 to 2.00. Thus, changes in their stability are related to the gradual increase in changes in entropy as related to the hydrogenation, from 107.7 to 116.5 J/mol H_2 K. We note that critical temperature gradually decreases following an increase of B/A.

Furthermore, the change of electrode potential has the similar values changing between with -0.9385 V for $AB_{1.9}$, -0.9505 V for $AB_{1.95}$, and -0.9652 V for $AB_{2.0}$.

When converted to the electrochemical capacity, this results in the capacities approaching 500 mAh/g for all three alloys. However, since the measurements of the capacity were performed using the open cells, the measured capacity were limited to the values corresponding to hydrogen pressures in gaseous phase of 1 bar H_2, even though in the close cells one can expect to achieve electrochemical capacities exceeding 500 mAh/g, depending on the applied hydrogen pressure.

In case of electrochemical capacity conversion, increasing the stoichiometry, capacity decreases from 568.5 mAh/g for $AB_{1.95}$ alloy, followed by 556.6 mAh/g for $AB_{1.9}$ alloy, and 508.1 mAh/g for $AB_{2.0}$ alloy (see Table 3, the data are taken from PCT modelling). It appeared that $AB_{1.95}$ alloy achieved the highest capacity among others which might be caused by the optimizing phase composition and structures obtained during annealing.

With regards to the interrelation between the gaseous and electrochemical capacities of the alloys, we note a good agreement between these two sets of the data. However, there are also some differences as the higher driving force causing the hydrogenation of the alloy during the electrochemical charging leads a higher absorption capacity of the metal hydride anode as compared to the experiments during studied of the metal-hydrogen gas interactions. Thus, the electrochemical capacity is slightly higher than the gaseous capacity. Furthermore, the potential plateau slope in electrochemical discharge curves is flatter and the plateau is longer as compared with the corresponding PCT diagrams while in addition α- and β-phases have longer homogeneity ranges in studied of the electrochemical characteristics.

5. Conclusions

❑ Annealed hypo-stoichiometric and stoichiometric $AB_{2-x}La_{0.03}$ Laves type alloys (A = $Ti_{0.15}Zr_{0.85}$; B= $Mn_{0.64-0.69}V_{0.11-0.119}Fe_{0.11-0.119}Ni_{1.097-1.184}$; x = 0, 0.05 and 0.1) were studied as materials for the metal hydride battery anodes. Their performance was characterized by metal-H_2 gas and electrochemically as metal hydride battery anodes;

❑ A significant increase of discharge capacity of AB_{2-x} with A = Zr, Ti, La, B= Ni, Fe, Mn, V and x = 0; 0.05 and 0.10, Laves type alloys was achieved by shifting alloys composition from hyper-stoichiometric $AB_{2.08}$ (420 mAh/g; reference data) [25,26] to hypo-stoichiometric $AB_{1.90}$ and $AB_{1.95}$ alloys (495 mAh/g; present study).

❑ Increasing B/A ratio (1.9, 1.95, and 2.0) significantly increases equilibrium pressure of hydrogen desorption, from 0.3 to 0.4 and 0.8 bar H_2 @ 293 K, while this change in composition of the alloys only slightly affects the enthalpy of hydrogen desorption, with all values being within a narrow interval between 34.0 and 35.2 kJ/mol H_2. Thus, decreasing of the stability of the hydrides is associated with a significant increase in the entropy change during the phase transformation which changes from 107.67 to 113.33 and 116.61 J/mol H_2 K, respectively. Furthermore, the critical temperature also continuously decreases from 386 to 370 and 366 K, while the hysteresis energy losses are increasing from 333 to 715 and 785 J/mol, respectively.

❑ $AB_{1.95}$ alloy showed the best activation performance with the best rate performance between all studied materials when high, 80% of the maximum, discharge capacity maintained at 500 mA/g (1 C) of applied current density.

❑ The stoichiometric $AB_{2.0}$ alloy showed an excellent cyclic stability associated with efficient hydrogen diffusion process which maintained practically unchanged after 500 cycles. During the cycling, hydrogen diffusion coefficients of the alloys show only marginal changes indicating that they maintain stable hydrogen transport characteristics.

❑ Some differences in hydrogen storage performance characterized by metal-H_2 gas interactions and electrochemically can be associated with reaching thermodynamic equilibrium during the PCT studies of the metal-H_2 systems in contrast to the dynamic process of hydrogen change and discharge in open cells applied during electrochemical characterization of the metal hydride anodes.

Declaration of competing interest

The authors declare that they have no known competing financial interests or personal relationships that could have appeared to influence the work reported in this paper.

CRediT authorship contribution statement

Ika Dewi Wijayanti: Writing - original draft, Writing - review & editing. **Roman Denys:** Writing - original draft. **Suwarno:** Writing - original draft. **Alexey A. Volodin:** Writing - original draft. **M.V. Lototskyy:** Formal analysis, Writing - original draft, Writing - review & editing. **Matylda N. Guzik:** Writing - original draft. **Jean Nei:** Writing - original draft. **Kwo Young:** Writing - original draft. **Hans Jørgen Roven:** Writing - original draft. **Volodymyr Yartys:** Writing - original draft, Writing - review & editing, Supervision, Formal analysis.

Acknowledgements

Appendix A. Supplementary data

Supplementary data to this article can be found online at https://doi.org/10.1016/j.jallcom.2020.154354.

References

[1] V. Yartys, D. Noreus, M. Latroche, Metal hydrides as negative electrode materials for Ni−MH batteries, Appl. Phys. A 122 (2016) 43.

[2] N. Furukawa, Development and commercialization of nickel-metal hydride secondary batteries, J. Power Sources 51 (1994) 45−59.

[3] M.L. Soria, J.n. Chacón, J.C. Hernández, D. Moreno, A. Ojeda, Nickel metal hydride batteries for high power applications, J. Power Sources 96 (2001) 68−75.

[4] M.A. Fetcenko, S.R. Ovshinsky, B. Reichman, K. Young, C. Fierro, J. Koch, A. Zallen, W. Mays, T. Ouchi, Recent advances in NiMH battery technology, J. Power Sources 165 (2007) 544−551.

[5] S. Tan, Y. Shen, E. Onur Şahin, D. Noréus, T. Öztürk, Activation behavior of an AB_2 type metal hydride alloy for NiMH batteries, Int. J. Hydrogen Energy 41 (2016) 9948−9953.

[6] K. Young, D.F. Wong, T. Ouchi, B. Huang, B. Reichman, Effects of La-addition to the structure, hydrogen storage, and electrochemical properties of C14 metal hydride alloys, Electrochim. Acta 174 (2015) 815−825.

[7] Y. Liu, H. Pan, M. Gao, Q. Wang, Advanced hydrogen storage alloys for Ni/MH rechargeable batteries, J. Mater. Chem. 21 (2011) 4743−4755.

[8] K.-H. Young, J. Nei, C. Wan, R. Denys, V. Yartys, Comparison of C14- and C15-predomiated AB2 metal hydride alloys for electrochemical applications, Batteries 3 (2017) 22.

[9] K.-H. Young, J.M. Koch, C. Wan, R.V. Denys, V.A. Yartys, Cell performance comparison between C14-and C15-predomiated AB_2 metal hydride alloys, Batteries 3 (2017) 29.

[10] D.-M. Kim, K.-J. Jang, J.-Y. Lee, A review on the development of AB_2-type Zr-based Laves phase hydrogen storage alloys for Ni−MH rechargeable batteries in the Korea Advanced Institute of Science and Technology, J. Alloys Compd. 293 (1999) 583−592.

[11] F. Cuevas, J.-M. Joubert, M. Latroche, A. Percheron-Guégan, Intermetallic compounds as negative electrodes of Ni/MH batteries, Appl. Phys. A 72 (2001) 225−238.

[12] H. Taizhong, W. Zhu, X. Baojia, X. Naixin, Effect of stoichiometry on hydrogen storage performance of Ti−Cr−VFe based alloys, Intermetallics 13 (2005) 1075−1078.

[13] T.A. Zotov, R.B. Sivov, E.A. Movlaev, S.V. Mitrokhin, V.N. Verbetsky, IMC hydrides with high hydrogen dissociation pressure, J. Alloys Compd. 509 (2011) S839−S843.

[14] S.R. Ovshinsky, M.A. Fetcenko, Development of high catalytic activity disordered hydrogen-storage alloys for electrochemical application in nickel−metal hydride batterie, Appl. Phys. A 72 (2001) 239−244.

[15] Y. Zhu, H. Pan, M. Gao, Y. Liu, Q. Wang, A study on improving the cycling stability of $(Ti_{0.8}Zr_{0.2})(V_{0.533}Mn_{0.107}Cr_{0.16}Ni_{0.2})_4$ hydrogen storage electrode alloy by means of annealing treatment: II. Effects on the electrochemical properties, J. Alloys Compd. 348 (2003) 301−308.

[16] J. Nei, K. Young, R. Regmi, G. Lawes, S.O. Salley, K.Y.S. Ng, Gaseous phase hydrogen storage and electrochemical properties of Zr_8Ni_{21}, Zr_7Ni_{10}, Zr_9Ni_{11}, and ZrNi metal hydride alloys, Int. J. Hydrogen Energy 37 (2012) 16042−16055.

[17] Y.L. Zhang, J.S. Li, T.B. Zhang, R. Hu, X.Y. Xue, Microstructure and hydrogen storage properties of non-stoichiometric Zr−Ti−V Laves phase alloys, Int. J. Hydrogen Energy 38 (2013) 14675−14684.

[18] F. Pourarian, H. Fujii, W. Wallace, V. Sinha, H.K. Smith, Stability and magnetism of hydrides of nonstoichiometric $ZrMn_2$, J. Phys. Chem. 85 (1981) 3105−3111.

[19] V.K. Sinha, F. Pourarian, W.E. Wallace, Hydrogenation characteristics of $Zr_{1−x}Ti_xMnFe$ alloys, J. Less Common Met. 87 (1982) 283−296.

[20] B.H. Liu, Z.P. Li, S. Suda, Electrochemical cycle life of Zr-based Laves phase alloys influenced by alloy stoichiometry and composition, J. Electrochem. Soc. 149 (2002) A537−A542.

[21] K. Young, J. Nei, B. Huang, M. Fetcenko, Studies of off-stoichiometric AB_2 metal hydride alloy: Part 2. Hydrogen storage and electrochemical properties, Int. J. Hydrogen Energy 36 (2011) 11146−11154.

[22] S.-M. Lee, H. Lee, J.-H. Kim, P.S. Lee, J.-Y. Lee, A study on the development of hypo-stoichiometric Zr-based hydrogen storage alloys with ultra-high capacity for anode material of Ni/MH secondary battery, J. Alloys Compd. 308 (2000) 259−268.

[23] I.D. Wijayanti, L. Mølmen, R.V. Denys, J. Nei, S. Gorsse, K. Young, M.N. Guzik, V. Yartys, The electrochemical performance of melt-spun C14-Laves type TiZr-based alloy, Int. J. Hydrogen Energy 45 (2020) 1297−1303.

[24] I.D. Wijayanti, L. Mølmen, R.V. Denys, J. Nei, S. Gorsse, M.N. Guzik, K. Young, V. Yartys, Studies of Zr-based C15 type metal hydride battery anode alloys prepared by rapid solidification, J. Alloys Compd. 804 (2019) 527−537.

[25] A.A. Volodin, R.V. Denys, C. Wan, I.D. Wijayanti, B.P. Tarasov, V.E. Antonov,

V.A. Yartys, Study of hydrogen storage and electrochemical properties of AB_2-type $Ti_{0.15}Zr_{0.85}La_{0.03}Ni_{1.2}Mn_{0.7}V_{0.12}Fe_{0.12}$ alloy, J. Alloys Compd. 793 (2019) 564−575.

[26] C. Wan, R. Denys, M. Lelis, D. Milčius, V. Yartys, Electrochemical studies and phase-structural characterization of a high-capacity La-doped AB_2 Laves type alloy and its hydride, J. Power Sources 418 (2019) 193−201.

[27] A.C. Larson, R. Von Dreele, General Structure Analysis System (GSAS)(Report LAUR 86-748), Los Alamos National Laboratory, Los Alamos, New Mexico, 2004.

[28] Y.L. Du, G. Chen, G.L. Chen, Optimization of Zr-based hydrogen storage alloys for nickel-hydride batteries, Intermetallics 13 (2005) 399−402.

[29] K. Shu, S. Zhang, Y. Lei, G. Lü, Q. Wang, Effect of Ti on the structure and electrochemical performance of Zr-based AB_2 alloys for nickel−metal rechargeable batteries, J. Alloys Compd. 349 (2003) 237−241.

[30] M. Lototskyy, New model of phase equilibria in metal−hydrogen systems: features and software, Int. J. Hydrogen Energy 41 (2016) 2739−2761.

[31] C.-N. Park, S. Luo, T.B. Flanagan, Analysis of sloping plateaux in alloys and intermetallic hydrides: I. Diagnostic features, J. Alloys Compd. 384 (2004) 203−207.

[32] Z. Szklarska-Smialowska, M. Smialowski, Electrochemical study of the nickel-hydrogen system, J. Electrochem. Soc. 110 (1963) 444−448.

[33] E.G. Ponyatovsky, V.E. Antonov, I.T. Belash, in: A.M. Prokhorov, A.S. Prokhorov (Eds.), High Hydrogen Pressures, Synthesis and Properties of New Hydrides, Problems in Solid State Physics, Mir Publ, Moscow, 1984, pp. 109−171.